# Full 3D Antenna Pattern Interpolation Using Fourier Transform Based Wavefield Modelling


Stephan Häfner, Robert Müller and Reiner S. Thomä
Electronic Measurement Engineering Group
Technische Universität Ilmenau
98684 Ilmenau, Germany
Email: stephan.haefner@tu-ilmenau.de



***Abstract*—A novel approach for model-based interpolation of sampled antenna pattern in azimuth, elevation and frequency domain is presented. Using wavefield modelling, an algebraic antenna model is derived, which incorporates Fourier transformation and is stated as Effective Time-Aperture Distribution Function (ETADF). A method to automatically de-noise sampled antenna pattern by estimating the model order is proposed. Furthermore, numerically efficient interpolation of antenna pattern data from the ETADF is presented. The ETADF approach is validated on simulation data of a conical horn antenna.**


## I. Introduction

Exact knowledge of the antenna radiation pattern is important for e.g. radio channel modelling, direction finding applications or antenna performance determination. As stated in literature, the radiation pattern depends on the direction as well as on the polarisation of excitation [1], [2] for narrowband applications. Furthermore, the radiation pattern becomes frequency dependent over the excited frequency band for wideband and ultra-wideband applications. Therefore, the antenna has to be known in angular, polarisation and frequency domain.

Sampled antenna patterns in angular and frequency domain are not sufficient, if the antenna pattern has to be known at arbitrary sampling points. Furthermore, storage saving representation of sampled antenna pattern and efficient reconstruction methods is quite important. Thus, an antenna model is required to efficiently reconstruct or interpolate the antenna pattern. For practical application, these models have to consider realistic antenna data to incorporate e.g. antenna imperfections and mutual coupling. Such models can be derived from wavefield modelling [3]. There, sampled antenna patterns are decomposed in a sampling matrix and a basis vector, why this kind of antenna models are stated as algebraic antenna models.

Known algebraic antenna models are the Effective Aperture Distribution Function (EADF) [4], the scalar spherical harmonics (SSH) [5], [6] or the vector spherical harmonics (VSH) [7], which are limited to angular and polarisation domain. Models which incorporate also the frequency domain are SSH with Padé approximant [8], VSH with Slepian mode expansion (SME) [9] or VSH with singularity expansion method (SEM) [10]. In this contribution the Effective Time-Aperture Distribution Function (ETADF) is presented, which extends the Fourier transform based EADF approach to incorporate the frequency domain (full 3D). Tensor algebra is used for compact presentation of the ETADF.

The rest of the paper is organized as follows: we introduce the basic antenna description and Fourier transform based wavefield modelling in Section II. Furthermore, analytical comparison of the ETADF approach with other full 3D wavefield modelling approaches is presented. Section III describes (i) the ETADF approach, (ii) a method for compression and denoising of ETADF data and (iii) calculation of antenna pattern derivatives for e.g. optimisation algorithms or performance measures like the Cramér-Rao bound. Efficient interpolation of the antenna pattern utilising the ETADF is presented in Section IV. A method to estimate the number of Fourier coefficients to sufficiently represent the antenna pattern will be given in Section V. The ETADF approach is validated in Section VI, by a comparison between simulated and reconstructed pattern of a conical horn antenna. Section VII concludes the paper.

Mathematical notation in this paper is as follows: scalars are italic lower-case letters, vectors (in column format, unless declared otherwise) are written as bold faced lower-case letters, matrices correspond to bold faced capitals, and tensors are bold faced calligraphic letters. We define the matrix operations $(.)^T$, $(.)^\dagger$ and $(.)^H$ as the transpose, pseudo-inverse and conjugate transpose of a matrix, respectively. The Frobenius-norm of a tensor is stated as $\|.\|_F$, see [11]. Real part and imaginary part of a complex number are depicted as $\Re\{.\}$ and $\Im\{.\}$, respectively. We define the q-mode product between a tensor $\boldsymbol{\mathcal{B}} \in \mathbb{C}^{M_1 \times \ldots \times M_q \times \ldots M_Q}$ and a matrix $\boldsymbol{A} \in \mathbb{C}^{P_q \times \ldots M_q}$ as $\boldsymbol{\mathcal{B}} \times_q \boldsymbol{A}$, which is obtained by multiplying the q-mode unfolding $\mathfrak{U}_{(q)}\{.\}$ (column-order in accordance with [11]) of the tensor from the left-hand side by the matrix and inverse unfolding: $\mathfrak{U}^{-1}_{(q)}\left\{\boldsymbol{A} \cdot \mathfrak{U}_{(q)}\{\boldsymbol{\mathcal{B}}\}\right\} \in \mathbb{C}^{M_1 \times \ldots \times P_q \times \ldots M_Q}$. Concatenation of two tensors along dimension $q$ is denoted by $\sqcup_q$.

## II. Antenna Description and Wavefield Modelling

We assume an antenna placed in the origin of a spherical coordinate system Figure 1. Spherical coordinates are defined by the elevation angle $\vartheta$ in the range from $[-\pi/2\ ,\ \pi/2]$ and the azimuth angle $\varphi$ in the range of $[-\pi, \pi]$. Polarisation of an impinging wave is defined according to the $\varphi$-$\vartheta$-plane, spanned by the spherical coordinate system basis vectors $\boldsymbol{k}_\varphi$ and $\boldsymbol{k}_\vartheta$ in the impingement point on the sphere.

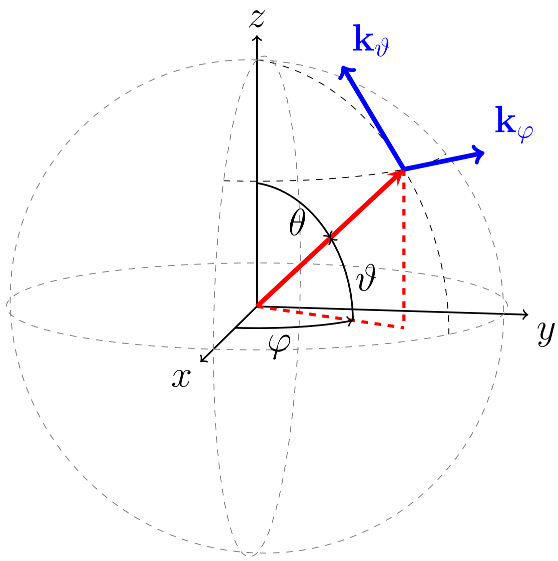


Figure 1. Spherical coordinate system and polarisation definition

Antennas are assumed as linear, time invariant systems [12] with a finite impulse response duration. Basically, an antenna is described by its radiated far-field electromagnetic wave $\boldsymbol{e}$ at distance $r$:

$$\begin{aligned}\boldsymbol{e}(\varphi,\vartheta,f) &= \frac{e^{-\jmath 2\pi r \frac{f}{c}}}{r}\begin{bmatrix}\boldsymbol{k}_\varphi & \boldsymbol{k}_\vartheta\end{bmatrix}\begin{bmatrix}b_\varphi(\varphi,\vartheta,f)\\ b_\vartheta(\varphi,\vartheta,f)\end{bmatrix}\\ &= \frac{e^{-\jmath 2\pi r \frac{f}{c}}}{r}\boldsymbol{K}_{\varphi,\vartheta}\boldsymbol{b}(\varphi,\vartheta,f) \qquad (1)\end{aligned}$$

with the speed of light $c$. An antenna is fully described by the polarimetric radiation pattern $\boldsymbol{b}(\varphi,\vartheta,f)$. In practise, this pattern is known at discrete sampling points in spherical coordinates, by e.g. measurements in an anechoic chamber or simulations. Off-grid sampling points can be derived from interpolation, which requires a proper antenna model.

An antenna model can be obtained from wavefield modelling [3], where the antenna manifold is expanded by orthogonal decomposition. Extending this idea to incorporate the frequency domain, the full 3D antenna pattern expansion is given by integral transformation:

$$b_{\varphi|\vartheta}(\boldsymbol{\omega}) = \int_{\mathbb{R}^3} g_{\varphi|\vartheta}(\boldsymbol{\mu})\cdot\psi(\boldsymbol{\mu};\boldsymbol{\omega})\,d\boldsymbol{\mu} \qquad (2)$$

with $\psi(\boldsymbol{\mu};\boldsymbol{\omega})$ the kernel function, $g_{\varphi|\vartheta}(\boldsymbol{\mu})$ the expansion coefficients, $\boldsymbol{\mu} = \begin{bmatrix}\mu_\varphi & \mu_\vartheta & \mu_f\end{bmatrix}^T$ the vector of expansion dimensions and $\boldsymbol{\omega} = \begin{bmatrix}\varphi & \vartheta & f\end{bmatrix}^T$ the vector of antenna dimensions. This integral transform describes each antenna dimension continuously and hence enables antenna pattern interpolation. Assuming orthogonality and self-reciprocity of the kernel function, the expansion coefficients are given by:

$$g_{\varphi|\vartheta}(\boldsymbol{\mu}) = \int_{\mathbb{R}^3} b_{\varphi|\vartheta}(\boldsymbol{\omega})\cdot\psi^H(\boldsymbol{\mu};\boldsymbol{\omega})\,d\boldsymbol{\omega} \qquad (3)$$

Kernel functions which fulfil the orthogonality and self-reciprocity condition are Fourier kernels, why wavefield modelling becomes Fourier transformation. Applicable Fourier transformations, in particular for the angular domain, are the cartesian Fourier transform (CFT) (see [4], [13]) and spherical Fourier transform (SFT) (see e.g. [5]–[7]). Extensions of SFT to consider the frequency domain are e.g. [8]–[10]. Subsequently, extension of the CFT to incorporate the frequency domain is presented, which is the basis to derive the ETADF in Section III. Furthermore, CFT and SFT based wavefield modelling are analytically compared w.r.t. the applied kernel functions for expansion.

### A. Cartesian Fourier transform based wavefield modelling

The kernel function $\boldsymbol{\psi}$ of the CFT in 3D is given by:

$$\psi(\mu_x,\mu_y,\mu_z;x,y,z) = e^{\jmath 2\pi\mu_x x}\cdot e^{\jmath 2\pi\mu_y y}\cdot e^{\jmath 2\pi\mu_z z} \qquad (4)$$

It is noticeable, that the 3-dimensional kernel function is given as the product of 1-dimensional kernel functions and therefore becomes easily computable.

Application of the CFT to data measured in spherical coordinates requires a projection of the spherical surface on a planar surface. Several projections are known from map projections, whereas the Plate Carrée projection [14] is applied here. This projection preserves equidistant spacing, which is a key assumption to apply CFT. The relation between spherical and Cartesian coordinates is:

$$\begin{aligned}\varphi &\to x\\ \vartheta &\to y\\ f &\to z\end{aligned}$$

### B. Comparison of CFT and SFT based wavefield modelling

Comparison of CFT and SFT based wavefield modelling is conducted according to the kernel functions in terms of i) suitability to describe an antenna pattern and ii) computational complexity. Note, that expansion of the frequency domain and angular domain are not related and therefore expansion in these domains can be compared separately.

First, CFT and SFT approach are compared according to their angular domain decomposition. Costa et.al. [13] showed, that the antenna manifold expansion in CFT and SFT are equivalent under some mild assumptions. Nevertheless, the CFT approach has some disadvantages due to the applied projection of the spherical surface on a planar surface. Tissot's indicatrix [15] can be used to visualise distortions introduced by map projections. Small circles of equal radii are placed at several sphere locations, which is projected on the map afterwards. Modification of the circles in size and shape indicate, whether the projection is non-equal-area or non-conformal, respectively. The Tissot indicatrix for the Plate Carrée projection is shown in Figure 2. Distortions do not occur for the circles of longitudes but for the circles of latitudes, because these circles are enlarged to the length of the equator. Therefore, the distortions increase to the poles,

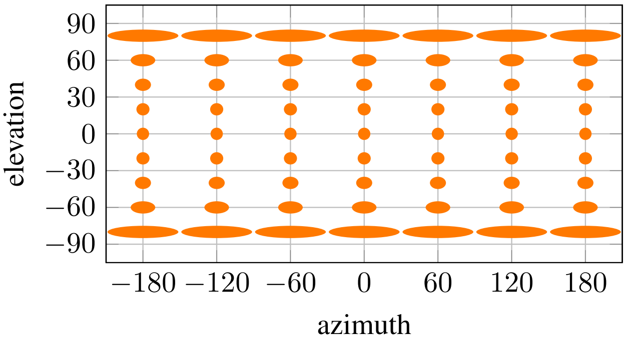


Figure 2. Tissot indicatrix for the Plate Carrée projection

which results in three findings w.r.t the CFT based wavefield modelling. First, projected data and their CFT are not rotation-invariant. Second, more expansion coefficients compared to the SFT approach are necessary for proper wavefield modelling. Third, the antenna main beam should coincide with the azimuth plane, because significant radiation power at the poles would require more coefficients for proper wavefield modelling. The SFT does not feature this limitations and therefore is more suitable for angular domain decomposition. On the contrary, antenna pattern interpolation using the SFT approach is computationally cumbersome, because the kernel functions are hard to compute numerically. Furthermore, calculation of derivatives w.r.t. the angles is computationally less complex for the CFT.

Second, CFT and SFT approach are compared according to their frequency domain expansion. Several frequency domain expansion methods are stated in literature for the SFT, like SME [9], SEM [10] or Padé approximation [8]. SME and SEM were compared in [9], showing that SME outperforms the SEM in terms of interpolation accuracy, calculation speed and noise sensitivity. Compared with the Fourier expansion in CFT, the Slepian expansion and Padé approximation are computationally much more cumbersome, because their kernel functions are difficult to calculate. Also, the bandwidth parameter for the Slepain expansion is not a fixed value and has to be determined by e.g. an optimisation algorithm [9].

Summarised, the CFT based wavefield modelling outperforms the SFT in terms of computational complexity, because the kernel function in angular and frequency domain is computationally less cumbersome. This becomes a major advantage, if the approaches are considered for algorithms, which require many antenna pattern interpolation steps.

## III. Effective Time-Aperture Distribution Function

Subsequently, a Fourier-based algebraic antenna model is described, which considers the previously introduced CFT wavefield modelling approach and a discrete set of sampled antenna radiation pattern. Thus, integral equation (3) is solved numerically, to derive the expansion coefficients. This cubature is calculated by discrete Fourier transform (DFT) of the sampled antenna pattern.

### A. Discrete Fourier transform of Antenna Pattern

The antenna radiation pattern is sampled according to the Nyquist criterion in azimuth steps $\Delta\varphi$, elevation steps $\Delta\vartheta$ and frequency steps $\Delta\nu$. The vectors of sampling points are give as:

$$\boldsymbol{\varphi} = \left[-\pi \dots \Delta\varphi \dots \pi - \Delta\varphi\right]^T \qquad \in \mathbb{R}^{L_1 \times 1} \tag{5}$$

$$\boldsymbol{\vartheta} = \left[\pi/2 \dots \Delta\vartheta \dots -\pi/2\right]^T \qquad \in \mathbb{R}^{L'_2 \times 1} \tag{6}$$

$$\boldsymbol{\nu} = \left[-B/2 \dots \Delta\nu \dots B/2 - \Delta\nu\right]^T \in \mathbb{R}^{L'_3 \times 1} \tag{7}$$

with $B$ being the bandwidth. The sampled antenna pattern per polarisation $k$ forms a tensor $\boldsymbol{\mathcal{B}}_k(\boldsymbol{\varphi}, \boldsymbol{\vartheta}, \boldsymbol{\nu}) \in \mathbb{C}^{L_1 \times L'_2 \times L'_3}$. Due to the orthogonality of the individual polarisation components, following investigations are limited to a single polarisation.

Subsequently, co-elevation $\theta$ instead of elevation is used with sampling vector $\boldsymbol{\theta}' = \left[0 \dots \Delta\vartheta \dots \pi\right]^T$. Furthermore, the normalised frequency sampling vector is introduced:

$$\boldsymbol{f}' = \pi \cdot \frac{\boldsymbol{\nu} - \min\{\boldsymbol{\nu}\}}{\max\{\boldsymbol{\nu}\} - \min\{\boldsymbol{\nu}\}} = \left[0 \dots \Delta f \dots \pi\right]^T \tag{8}$$

The sampled antenna pattern is only periodic in azimuth domain. Hence, in order to avoid truncation errors during DFT, periodic extension of the elevation domain [4] and the frequency domain is necessary. Calculation of the periodical antenna pattern $\boldsymbol{\mathcal{B}}_k^{(p)}(\boldsymbol{\varphi}, \boldsymbol{\theta}, \boldsymbol{f}) \in \mathbb{C}^{L_1 \times L_2 \times L_3}$ is given in equation (9), with $\boldsymbol{\theta} = \left[-\pi + \Delta\theta \dots \Delta\theta \dots \pi\right]^T$ and $\boldsymbol{f} = \left[-\pi + \Delta f \dots \Delta f \dots \pi\right]^T$ being the sampling vectors of the periodic antenna pattern in co-elevation and frequency domain, respectively.

Utilising the periodic antenna pattern, the antenna pattern's DFT is given by:

$$\boldsymbol{\mathcal{G}}_k = \boldsymbol{\mathcal{B}}_k^{(p)}(\boldsymbol{\varphi}, \boldsymbol{\theta}, \boldsymbol{f}) \times_1 \boldsymbol{E}(\boldsymbol{\varphi}) \times_2 \boldsymbol{E}(\boldsymbol{\theta}) \times_3 \boldsymbol{E}(\boldsymbol{f}) \tag{10}$$

$$\begin{aligned}\boldsymbol{\mathcal{B}}_k^{(p)}(\boldsymbol{\varphi}, \boldsymbol{\theta}, \boldsymbol{f}) = &\left[-\left(\boldsymbol{\mathcal{B}}_k(\boldsymbol{\varphi}', \boldsymbol{\theta}'', \boldsymbol{f}'') \sqcup_1 \boldsymbol{\mathcal{B}}_k(\boldsymbol{\varphi}'', \boldsymbol{\theta}'', \boldsymbol{f}'')\right) \sqcup_2 \boldsymbol{\mathcal{B}}_k(\boldsymbol{\varphi}, \boldsymbol{\theta}', \boldsymbol{f}'')\right] \\ &\sqcup_3 \left[-\left(\boldsymbol{\mathcal{B}}_k(\boldsymbol{\varphi}', \boldsymbol{\theta}'', \boldsymbol{f}') \sqcup_1 \boldsymbol{\mathcal{B}}_k(\boldsymbol{\varphi}'', \boldsymbol{\theta}'', \boldsymbol{f}')\right) \sqcup_2 \boldsymbol{\mathcal{B}}_k(\boldsymbol{\varphi}, \boldsymbol{\theta}', \boldsymbol{f}')\right]\end{aligned} \tag{9}$$

$$\boldsymbol{\theta}'' = \left[\pi - \Delta\theta \dots \Delta\theta\right]^T \qquad \boldsymbol{\varphi}' = \left[0 \dots \pi - \Delta\varphi\right]^T$$

$$\boldsymbol{\varphi}'' = \left[-\pi \dots -\Delta\varphi\right]^T \qquad \boldsymbol{f}'' = \left[\pi - \Delta f \dots \Delta f\right]^T$$

with the DFT matrices

$$\boldsymbol{E}(\boldsymbol{\varphi}) = \left(e^{\jmath \boldsymbol{\varphi} \boldsymbol{\mu}_\varphi^T}\right)^\dagger \quad \in \mathbb{C}^{L_1 \times L_1} \tag{11a}$$

$$\boldsymbol{E}(\boldsymbol{\theta}) = \left(e^{\jmath \boldsymbol{\theta} \boldsymbol{\mu}_\theta^T}\right)^\dagger \quad \in \mathbb{C}^{L_2 \times L_2} \tag{11b}$$

$$\boldsymbol{E}(\boldsymbol{f}) = \left(e^{\jmath \boldsymbol{f} \boldsymbol{\mu}_f^T}\right)^\dagger \quad \in \mathbb{C}^{L_3 \times L_3} \tag{11c}$$

$$\boldsymbol{\mu}_\varphi = \left[-\tfrac{L_1}{2} \dots \tfrac{L_1}{2} - 1\right]^T \in \mathbb{R}^{L_1 \times 1}$$

$$\boldsymbol{\mu}_\theta = \left[-\tfrac{L_2}{2} \dots \tfrac{L_2}{2} - 1\right]^T \in \mathbb{R}^{L_2 \times 1}$$

$$\boldsymbol{\mu}_f = \left[-\tfrac{L_3}{2} \dots \tfrac{L_3}{2} - 1\right]^T \in \mathbb{R}^{L_3 \times 1}$$

Tensor $\boldsymbol{\mathcal{G}}_k$ contains the Fourier coefficients and is stated as the Time-Aperture Distribution Function (TADF) of the antenna for polarisation $k$.

Considering the TADF, the Fourier-based algebraic antenna model for each polarisation $k$ is given as:

$$b_k(\varphi, \theta, f) = \boldsymbol{\mathcal{G}}_k \times_1 \boldsymbol{d}(\varphi) \times_2 \boldsymbol{d}(\theta) \times_3 \boldsymbol{d}(f) \tag{12}$$

with $\boldsymbol{d}$ the inverse discrete Fourier transform (iDFT) row-vectors per dimension.

### B. Compression and De-Noising

Naturally, the Fourier transformed angular domain is band limited [3], [4] and, because we assumed a finite antenna impulse response duration, the same holds for the Fourier transformed frequency domain. Furthermore, if the antenna pattern is oversampled, their Fourier transformation is also band limited. Hence, a finite number of Fourier coefficients is sufficient for accurate antenna pattern modelling. The TADF can be compressed to energy carrying Fourier coefficients, whereas noise carrying coefficients can be truncated.

Compression of the TADF has several advantages. First, the amount of data to store is reduced. Second, because noise carrying signal parts are dropped, the measured data are de-noised. Last, the computational complexity of the antenna interpolation (see next section) is reduced, because less data points have to be considered. Therefore, the compressed version of the TADF is called ETADF.

Calculation of the ETADF is possible by truncating the DFT matrices. The truncated DFT matrices are:

$$\bar{\boldsymbol{E}}(\boldsymbol{\varphi}) = \left(e^{\jmath \boldsymbol{\varphi} \bar{\boldsymbol{\mu}}_\varphi}\right)^\dagger \quad \in \mathbb{C}^{N_1 \times L_1} \tag{13a}$$

$$\bar{\boldsymbol{E}}(\boldsymbol{\theta}) = \left(e^{\jmath \boldsymbol{\theta} \bar{\boldsymbol{\mu}}_\theta}\right)^\dagger \quad \in \mathbb{C}^{N_2 \times L_2} \tag{13b}$$

$$\bar{\boldsymbol{E}}(\boldsymbol{f}) = \left(e^{\jmath \boldsymbol{f} \bar{\boldsymbol{\mu}}_f}\right)^\dagger \quad \in \mathbb{C}^{N_3 \times L_3} \tag{13c}$$

$$\bar{\boldsymbol{\mu}}_\varphi = \left[-\tfrac{N_1-1}{2} \dots \tfrac{N_1-1}{2}\right] \in \mathbb{R}^{1 \times N_1}$$

$$\bar{\boldsymbol{\mu}}_\theta = \left[-\tfrac{N_2-1}{2} \dots \tfrac{N_2-1}{2}\right] \in \mathbb{R}^{1 \times N_2}$$

$$\bar{\boldsymbol{\mu}}_f = \left[-\tfrac{N_3-1}{2} \dots \tfrac{N_3-1}{2}\right] \in \mathbb{R}^{1 \times N_3}$$

with $N_1, N_2, N_3$ are odd numbers, with $N_1 < L_1$, $N_2 < L_2$, $N_3 < L_3$ for truncation. The ETADF for polarisation $k$ is:

$$\bar{\boldsymbol{\mathcal{G}}}_k = \boldsymbol{\mathcal{B}}_k^{(p)}(\boldsymbol{\varphi}, \boldsymbol{\theta}, \boldsymbol{f}) \times_1 \bar{\boldsymbol{E}}(\boldsymbol{\varphi}) \times_2 \bar{\boldsymbol{E}}(\boldsymbol{\theta}) \times_3 \bar{\boldsymbol{E}}(\boldsymbol{f}) \tag{14}$$

An ETADF tensor is visualised in Figure 3. The yellow fields refer to tensor entries, where $\mu_\varphi = 0$, $\mu_\vartheta = 0$ or $\mu_f = 0$ holds.

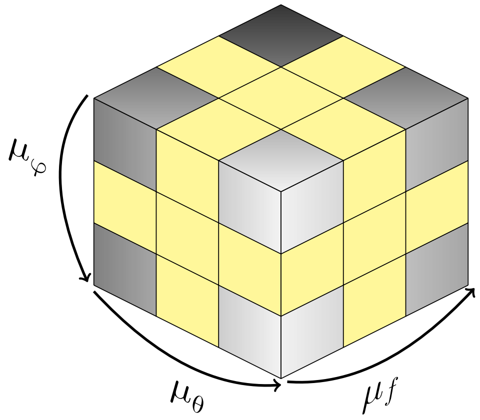


Figure 3. ETADF tensor $\bar{\boldsymbol{\mathcal{G}}}_k$ with yellow sub-tensors where $\mu_\varphi = 0$, $\mu_\vartheta = 0$ or $\mu_f = 0$ holds

### C. Antenna Pattern Differential

Utilising the Fourier-based algebraic antenna model (12) and application of the product rule, the partial derivative of the antenna pattern w.r.t. azimuth $\varphi$ becomes:

$$\begin{aligned}\frac{\partial}{\partial \varphi} b_k(\varphi, \theta, f) &= \bar{\boldsymbol{\mathcal{G}}}_k \times_1 \frac{\partial}{\partial \varphi} \boldsymbol{d}(\varphi) \times_2 \boldsymbol{d}(\theta) \times_3 \boldsymbol{d}(f) \\ &= \bar{\boldsymbol{\mathcal{G}}}_k \times_1 \boldsymbol{d}(\varphi) \cdot \boldsymbol{U}(\varphi) \times_2 \boldsymbol{d}(\theta) \times_3 \boldsymbol{d}(f)\end{aligned} \tag{15}$$

with the iDFT row-vectors:

$$\boldsymbol{d}(\varphi) = e^{\jmath(\boldsymbol{\mu}_\varphi \varphi)} \quad \in \mathbb{C}^{1 \times N_1} \tag{16a}$$

$$\boldsymbol{d}(\theta) = e^{\jmath(\boldsymbol{\mu}_\theta \theta)} \quad \in \mathbb{C}^{1 \times N_2} \tag{16b}$$

$$\boldsymbol{d}(f) = e^{\jmath(\boldsymbol{\mu}_f f)} \quad \in \mathbb{C}^{1 \times N_3} \tag{16c}$$

$$\boldsymbol{\mu}_\varphi = \left[-\tfrac{N_1-1}{2} \dots \tfrac{N_1-1}{2}\right] \in \mathbb{R}^{1 \times N_1}$$

$$\boldsymbol{\mu}_\theta = \left[-\tfrac{N_2-1}{2} \dots \tfrac{N_2-1}{2}\right] \in \mathbb{R}^{1 \times N_2}$$

$$\boldsymbol{\mu}_f = \left[-\tfrac{N_3-1}{2} \dots \tfrac{N_3-1}{2}\right] \in \mathbb{R}^{1 \times N_3}$$

and diagonal matrix $\boldsymbol{U}(\varphi)$, containing the partial derivatives of the iDFT row-vector in azimuth:

$$\boldsymbol{U}(\varphi) = \operatorname{diag}\left\{\jmath \boldsymbol{\mu}_\varphi\right\} \tag{17}$$

Because matrix $\boldsymbol{U}(\varphi)$ is fixed, pre-multiplication with the ETADF tensor to save computation time is applied. Defining

$$\bar{\boldsymbol{\mathcal{G}}}_k^{\partial_\varphi} = \bar{\boldsymbol{\mathcal{G}}}_k \times_1 \boldsymbol{U}(\varphi) \tag{18}$$

the partial derivative in azimuth becomes:

$$\frac{\partial}{\partial \varphi} b_k(\varphi, \theta, f) = \bar{\boldsymbol{\mathcal{G}}}_k^{\partial_\varphi} \times_1 \boldsymbol{d}(\varphi) \times_2 \boldsymbol{d}(\theta) \times_3 \boldsymbol{d}(f) \tag{19}$$

Partial derivative w.r.t. elevation can be derived similarly and is not stated here.

## IV. Efficient Antenna Pattern Interpolation

Utilising the ETADF, reconstruction and interpolation of the antenna radiation pattern (and also its differential) is possible by iDFT [3]. The iDFT row-vectors (16a), (16b), (16c) are built according to the azimuth $\varphi_0$, co-elevation $\theta_0$

and normalised frequency $f_0$ of interest. Applying the iDFT row-vectors to the ETADF tensor, the antenna radiation pattern for polarisation $k$ is calculated as follows:

$$b_k(\varphi_0, \theta_0, f_0) = \bar{\boldsymbol{\mathcal{G}}}_k \times_1 \boldsymbol{d}(\varphi_0) \times_2 \boldsymbol{d}(\theta_0) \times_3 \boldsymbol{d}(f_0) \tag{20}$$

Calculating the antenna pattern using the above formula requires $\mathcal{O}(4N_1N_2N_3)$ real-valued multiplications and thus becoming rapidly computationally cumbersome. Therefore, methods for efficient calculation are necessary. In the following, a two stage approach is presented to 1) reduce the number of real-valued multiplications and 2) skipping redundancy, which allows a much more efficient calculation.

### A. Reducing of Multiplications

Due to the symmetry property of the iDFT vectors, the number of real-valued multiplications are reducible [16]. Generally, this property can be written as:

$$\boldsymbol{d} = \begin{bmatrix} (\boldsymbol{\Pi} \cdot \boldsymbol{a})^H & 1 & \boldsymbol{a}^T \end{bmatrix}^T$$
$$\boldsymbol{a} = \begin{bmatrix} e^{\jmath v} \dots e^{\jmath \frac{N-1}{2} v} \end{bmatrix}^T$$

with the permutation matrix $\boldsymbol{\Pi}$ as:

$$\boldsymbol{\Pi} = \begin{bmatrix} 0 & \dots & 1 \\ & \ddots & \\ 1 & \dots & 0 \end{bmatrix}$$

Due to this symmetry, the inner product of vector $\boldsymbol{d}$ and an arbitrary vector $\boldsymbol{w} = \begin{bmatrix} \boldsymbol{x}^T & y & \boldsymbol{z}^T \end{bmatrix}^T$ can be simplified as follows:

$$\boldsymbol{d}^T \cdot \boldsymbol{w} = \begin{bmatrix} 1 & \Re\{\boldsymbol{a}^T\} & \jmath\Im\{\boldsymbol{a}^T\} \end{bmatrix} \cdot \begin{bmatrix} y \\ \boldsymbol{z} + \boldsymbol{\Pi} \cdot \boldsymbol{x} \\ \boldsymbol{z} - \boldsymbol{\Pi} \cdot \boldsymbol{x} \end{bmatrix}$$

The number of real-valued multiplications is reduced by half. Vector $\boldsymbol{w}$ is folded by either summation or subtraction of his left and right part.

This relationship is utilised to reduce the computational complexity of the iDFT. First, we define the folding matrix $\boldsymbol{F}$:

$$\boldsymbol{F}(N) = \begin{bmatrix} \boldsymbol{o}^T_{\frac{N-1}{2}} & 1 & \boldsymbol{o}^T_{\frac{N-1}{2}} \\ \boldsymbol{\Pi}_{\frac{N-1}{2}} & \boldsymbol{o}_{\frac{N-1}{2}} & \boldsymbol{I}_{\frac{N-1}{2}} \\ -\jmath\boldsymbol{\Pi}_{\frac{N-1}{2}} & \boldsymbol{o}_{\frac{N-1}{2}} & \jmath\boldsymbol{I}_{\frac{N-1}{2}} \end{bmatrix} \in \mathbb{R}^{N \times N} \tag{21}$$

with $\boldsymbol{I}_N \in \mathbb{R}^{N \times N}$ the identity matrix and $\boldsymbol{o}_N \in \mathbb{R}^{N \times 1}$ vector of zero values. The ETADF folding is now given by:

$$\tilde{\bar{\boldsymbol{\mathcal{G}}}}_k = \bar{\boldsymbol{\mathcal{G}}}_k \times_1 \boldsymbol{F}(N_1) \times_2 \boldsymbol{F}(N_2) \times_3 \boldsymbol{F}(N_3) \tag{22}$$

with $\tilde{\bar{\boldsymbol{\mathcal{G}}}}_k \in \mathbb{C}^{N_1 \times N_2 \times N_3}$ the folded ETADF. A folded ETADF tensor is depicted in Figure 4, whereas the yellow blocks represent the sub-tensors where $\mu_\varphi = 0$, $\mu_\vartheta = 0$ or $\mu_f = 0$ holds.

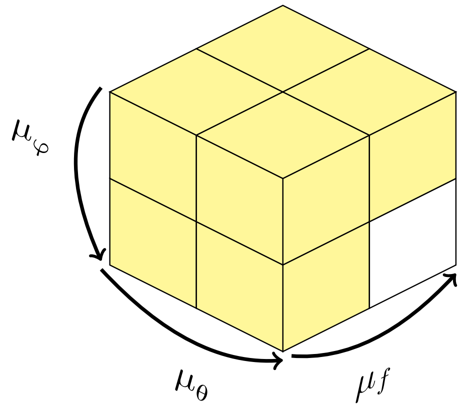


Figure 4. Folded ETADF tensor $\tilde{\bar{\boldsymbol{\mathcal{G}}}}_k$ with yellow sub-tensors where $\mu_\varphi = 0$, $\mu_\vartheta = 0$ or $\mu_f = 0$ holds

The antenna radiation pattern for polarisation $k$ can now be calculated by:

$$\begin{aligned} b_k(\varphi_0, \theta_0, f_0) &= \bar{\boldsymbol{\mathcal{G}}}_k \times_1 \boldsymbol{d}(\varphi_0) \times_2 \boldsymbol{d}(\theta_0) \times_3 \boldsymbol{d}(f_0) \\ &= \tilde{\bar{\boldsymbol{\mathcal{G}}}}_k \times_1 \tilde{\boldsymbol{d}}(\varphi_0) \times_2 \tilde{\boldsymbol{d}}(\theta_0) \times_3 \tilde{\boldsymbol{d}}(f_0) \end{aligned} \tag{23}$$

with the iDFT row-vectors:

$$\tilde{\boldsymbol{d}}(\varphi_0) = \begin{bmatrix} 1 & \Re\{e^{\jmath \tilde{\boldsymbol{\mu}}_\varphi \varphi_0}\} & \Im\{e^{\jmath \tilde{\boldsymbol{\mu}}_\varphi \varphi_0}\} \end{bmatrix} \in \mathbb{R}^{1 \times N_1} \tag{24a}$$
$$\tilde{\boldsymbol{d}}(\theta_0) = \begin{bmatrix} 1 & \Re\{e^{\jmath \tilde{\boldsymbol{\mu}}_\theta \theta_0}\} & \Im\{e^{\jmath \tilde{\boldsymbol{\mu}}_\theta \theta_0}\} \end{bmatrix} \in \mathbb{R}^{1 \times N_2} \tag{24b}$$
$$\tilde{\boldsymbol{d}}(\varphi_0) = \begin{bmatrix} 1 & \Re\{e^{\jmath \tilde{\boldsymbol{\mu}}_f f_0}\} & \Im\{e^{\jmath \tilde{\boldsymbol{\mu}}_f f_0}\} \end{bmatrix} \in \mathbb{R}^{1 \times N_3} \tag{24c}$$
$$\tilde{\boldsymbol{\mu}}_\varphi = \begin{bmatrix} 1 \dots \frac{N_1-1}{2} \end{bmatrix} \in \mathbb{R}^{1 \times \frac{N_1-1}{2}}$$
$$\tilde{\boldsymbol{\mu}}_\theta = \begin{bmatrix} 1 \dots \frac{N_2-1}{2} \end{bmatrix} \in \mathbb{R}^{1 \times \frac{N_2-1}{2}}$$
$$\tilde{\boldsymbol{\mu}}_f = \begin{bmatrix} 1 \dots \frac{N_3-1}{2} \end{bmatrix} \in \mathbb{R}^{1 \times \frac{N_3-1}{2}}$$

The number of real-valued multiplications is reduced to $\mathcal{O}(2N_1N_2N_3)$.

### B. Skipping of Redundancies

Due to the periodical extension of the radiation pattern in elevation and frequency domain, redundant data are added in azimuth domain [16]. This results in zero valued samples in the folded ETADF, which are negligible during iDFT calculation.

First, matrices $\boldsymbol{S}_e$ and $\boldsymbol{S}_o$ are introduced, which selects even and odd rows of a matrix, respectively:

$$\boldsymbol{S}_e = \begin{bmatrix} 0 & 1 & 0 & 0 & \dots & 0 & 0 \\ 0 & 0 & 0 & 1 & \dots & 0 & 0 \\ & & & & \vdots & & \\ 0 & 0 & 0 & 0 & \dots & 1 & 0 \end{bmatrix} \in \mathbb{R}^{\frac{N_1-1}{2} \times N_1} \tag{25}$$

$$\boldsymbol{S}_o = \begin{bmatrix} 1 & 0 & 0 & 0 & \dots & 0 & 0 \\ 0 & 0 & 1 & 0 & \dots & 0 & 0 \\ & & & & \vdots & & \\ 0 & 0 & 0 & 0 & \dots & 0 & 1 \end{bmatrix} \in \mathbb{R}^{\frac{N_1+1}{2} \times N_1} \tag{26}$$

Second, matrices $\boldsymbol{S}_u$ and $\boldsymbol{S}_l$ are introduced, which selects the upper and lower rows of a matrix, respectively:

$$\boldsymbol{S}_u(N) = \begin{bmatrix}\boldsymbol{I}_{\frac{N+1}{2}} & \boldsymbol{O}_{\frac{N+1}{2},\frac{N-1}{2}}\end{bmatrix} \in \mathbb{R}^{\frac{N+1}{2}\times N} \tag{27}$$

$$\boldsymbol{S}_l(N) = \begin{bmatrix}\boldsymbol{O}_{\frac{N-1}{2},\frac{N+1}{2}} & \boldsymbol{I}_{\frac{N-1}{2}}\end{bmatrix} \in \mathbb{R}^{\frac{N-1}{2}\times N} \tag{28}$$

with $\boldsymbol{O}_{A,B} \in \mathbb{R}^{A\times B}$ matrix of all zeros. For short hand notation, we abbreviate the multiplication of the selection matrices with the folded ETADF:

$$\tilde{\bar{\boldsymbol{\mathcal{G}}}}_k^e = \tilde{\bar{\boldsymbol{\mathcal{G}}}}_k \times_1 \boldsymbol{S}_e \times_2 \boldsymbol{S}_u(N_2) \times_3 \boldsymbol{S}_u(N_3) \in \mathbb{C}^{\frac{N_1-1}{2}\times\frac{N_2+1}{2}\times\frac{N_3+1}{2}} \tag{29}$$

$$\tilde{\bar{\boldsymbol{\mathcal{G}}}}_k^o = \tilde{\bar{\boldsymbol{\mathcal{G}}}}_k \times_1 \boldsymbol{S}_o \times_2 \boldsymbol{S}_l(N_2) \times_3 \boldsymbol{S}_u(N_3) \in \mathbb{C}^{\frac{N_1+1}{2}\times\frac{N_2-1}{2}\times\frac{N_3+1}{2}} \tag{30}$$

and the iDFT row-vectors:

$$\tilde{\boldsymbol{d}}_e(\varphi_0) = \tilde{\boldsymbol{d}}(\varphi_0)\cdot\boldsymbol{S}_e^T \quad \in \mathbb{R}^{1\times\frac{N_1-1}{2}} \tag{31a}$$

$$\tilde{\boldsymbol{d}}_o(\varphi_0) = \tilde{\boldsymbol{d}}(\varphi_0)\cdot\boldsymbol{S}_o^T \quad \in \mathbb{R}^{1\times\frac{N_1+1}{2}} \tag{31b}$$

$$\tilde{\boldsymbol{d}}_u(\theta_0) = \tilde{\boldsymbol{d}}(\theta_0)\cdot\boldsymbol{S}_u(N_2)^T \in \mathbb{R}^{1\times\frac{N_2+1}{2}} \tag{31c}$$

$$\tilde{\boldsymbol{d}}_l(\theta_0) = \tilde{\boldsymbol{d}}(\theta_0)\cdot\boldsymbol{S}_l(N_2)^T \in \mathbb{R}^{1\times\frac{N_2-1}{2}} \tag{31d}$$

$$\tilde{\boldsymbol{d}}_u(f_0) = \tilde{\boldsymbol{d}}(f_0)\cdot\boldsymbol{S}_u(N_3)^T \in \mathbb{R}^{1\times\frac{N_3+1}{2}} \tag{31e}$$

The antenna radiation pattern for polarisation $k$ is now given by:

$$\begin{aligned} b_k(\varphi_0,\theta_0,f_0) &= \bar{\boldsymbol{\mathcal{G}}}_k \times_1 \boldsymbol{d}(\varphi_0) \times_2 \boldsymbol{d}(\theta_0) \times_3 \boldsymbol{d}(f_0) \\ &= \tilde{\bar{\boldsymbol{\mathcal{G}}}}_k^e \times_1 \tilde{\boldsymbol{d}}_e(\varphi_0) \times_2 \tilde{\boldsymbol{d}}_u(\theta_0) \times_3 \tilde{\boldsymbol{d}}_u(f_0) \\ &\quad + \tilde{\bar{\boldsymbol{\mathcal{G}}}}_k^o \times_1 \tilde{\boldsymbol{d}}_o(\varphi_0) \times_2 \tilde{\boldsymbol{d}}_l(\theta_0) \times_3 \tilde{\boldsymbol{d}}_u(f_0) \end{aligned} \tag{32}$$

Due to the skipped redundancy, the number of real-valued multiplications is $\mathcal{O}(\frac{1}{2}\cdot N_1N_2N_3)$.

## V. Model Order Estimation

For de-noising purpose, the number of significant Fourier coefficients in each TADF dimension have to be determined. This topic can be considered as a model order estimation problem.

Due to the algebraic antenna model (12), unfolding of antenna dimension $q$ is:

$$\mathfrak{U}_{(q)}\left\{\boldsymbol{\mathcal{B}}_k^{(p)}\right\} = \boldsymbol{E}_{(q)} \cdot \mathfrak{U}_{(q)}\left\{\boldsymbol{\mathcal{G}}_k\right\} + \boldsymbol{N} \tag{33}$$

with $\boldsymbol{N} \sim \mathcal{N}(\boldsymbol{0}, \sigma_q^2\boldsymbol{I})$ the matrix of circular, normal distributed noise; $\mathfrak{U}_{(q)}\left\{\boldsymbol{\mathcal{G}}_k\right\}$ the unfolded TADF and $\boldsymbol{E}_{(q)}$ the DFT matrix. For notational convenience, following abbreviations are introduced:

$$\boldsymbol{B}_{k,(q)} = \mathfrak{U}_{(q)}\left\{\boldsymbol{\mathcal{B}}_k^{(p)}\right\} \in \mathbb{C}^{L_q\times\bar{L}_q} \tag{34}$$

$$\boldsymbol{G}_{k,(q)} = \mathfrak{U}_{(q)}\left\{\boldsymbol{\mathcal{G}}_k\right\} \quad \in \mathbb{C}^{L_q\times\bar{L}_q} \tag{35}$$

whereas $\bar{L}_q = \prod_{i=1,i\neq q}^3 L_i$. Thus, equation (33) becomes:

$$\boldsymbol{B}_{k,(q)} = \boldsymbol{E}_{(q)} \cdot \boldsymbol{G}_{k,(q)} + \boldsymbol{N} \tag{36}$$

Model (36) is decomposed into two parts, to account for $P_q$ significant and $L_q - P_q$ truncated Fourier coefficients:

$$\begin{aligned} \boldsymbol{B}_{k,(q)} &= \sum_{l=1}^{P_q} \boldsymbol{E}_{(q)}(:,l)\cdot\boldsymbol{G}_{k,(q)}(l,:) \\ &\quad + \sum_{l=1+P_q}^{L_q} \boldsymbol{E}_{(q)}(:,l)\cdot\boldsymbol{G}_{k,(q)}(l,:) + \boldsymbol{N} \end{aligned} \tag{37}$$

whereas $\boldsymbol{E}_{(q)}(:,l)$ denotes the selection of the $l$-th column and $\boldsymbol{G}_{k,(q)}(l,:)$ the selection of the $l$-th row. Decomposition of model (36) is accomplished by considering the first $P_q$ Fourier coefficients, which are ordered descendent according to their magnitude, and their corresponding DFT matrix vectors. Estimation of the model order is conducted by statistical comparison of model orders $P_q$ and $P_q + 1$. The additional Fourier coefficients are tested, whether they significantly differ from zero, why the test's $\mathcal{H}_0$ hypothesis is: $\boldsymbol{G}_{k,(q)}(P_q+1,:)^T = \boldsymbol{o}_{\bar{L}_q}$. If the $\mathcal{H}_0$ hypothesis is accepted, additional Fourier coefficients are not significantly different from zero and therefore negligible.

A suitable statistical test is the F-test [17, p. 37]. The test statistic $F_{stat}(P_q)$ for model order $P_q$ is:

$$F_{stat}(P_q) = \frac{\mathcal{L}(P_q) - \mathcal{L}(P_q+1)}{\mathcal{L}(P_q+1)}\cdot(L_q - P_q - 1) \tag{38}$$

The Fisher statistic is tested against the $1-\alpha$ percentile point $F_{1-\alpha}$ of the Fisher distribution, in order to verify the $\mathcal{H}_0$ hypothesis:

$$F_{stat}(P_q) < F_{1-\alpha}(2\cdot\bar{L}_q, 2\cdot\bar{L}_q\cdot(L_q - P_q - 1)) \tag{39}$$

with $\mathcal{L}(P_q)$ the sum of squared residuals according to model order $P_q$:

$$\begin{aligned} \mathcal{L}(P_q) &= \left\|\boldsymbol{B}_{k,(q)} - \boldsymbol{E}_{(q)}^{(P_q)}\boldsymbol{E}_{(q)}^{(P_q)\dagger}\boldsymbol{B}_{k,(q)}\right\|_F^2 \\ \boldsymbol{E}_{(q)}^{(P_q)} &= \boldsymbol{E}_{(q)}(:,1:P_q) \end{aligned} \tag{40}$$

Model orders from $P_q = 1...L_q - 1$ are successively tested, until $\mathcal{H}_0$ hypothesis cannot be rejected based on a significance level $\alpha$.

## VI. Simulation

The ETADF approach is validated on simulation data of a conical horn antenna (see Figure 5). Simulations were carried out with finite element tool ANSYS HFSS. The numerically calculated antenna pattern was sampled with $1^\circ$ in azimuth and elevation, and 10 MHz in frequency. The frequency ranged from 71 GHz to 78 GHz. Both polarisations were captured, whereas only $k_\vartheta$, the co-polarisation in main-beam direction, will be utilised for the investigations.

The tensor toolbox [18] was utilised for MatLab implementation of the ETADF approach.

In the following, analysis of the antenna pattern reconstruction error for different ETADF sizes is presented. As stated, the

Figure 5. ANSYS HFSS model of the conical horn antenna

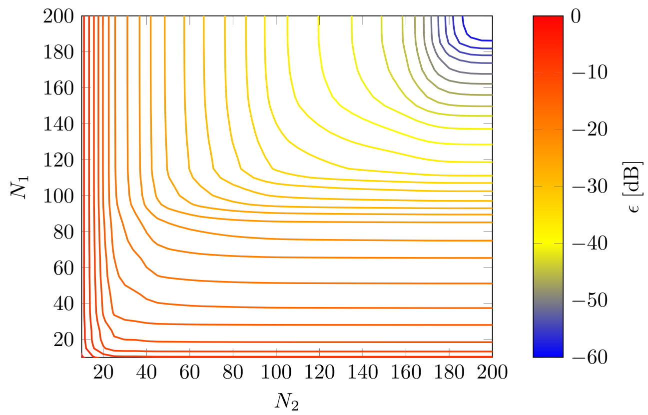


Figure 6. Reconstruction error $\epsilon$ for different compression sizes in azimuth ($N_1$) and elevation ($N_2$), fixed compression size $N_3 = 100$ in frequency

ETADF is calculated from the TADF by truncation of Fourier coefficients. The reconstruction error is defined as follows:

$$\epsilon = \frac{\left\| \boldsymbol{\mathcal{B}}_k^{sim} - \boldsymbol{\mathcal{B}}_k^{rec} \right\|_F^2}{\left\| \boldsymbol{\mathcal{B}}_k^{sim} \right\|_F^2} \tag{41}$$

with $\boldsymbol{\mathcal{B}}_k^{sim}$ and $\boldsymbol{\mathcal{B}}_k^{rec}$ being the simulated and reconstructed antenna pattern, respectively.

The reconstruction error for varying compression sizes in azimuth and elevation, and fixed compression $N_3 = 100$ in frequency, is depicted in Figure 6. As visible, a compression size of approx. $N_1 = N_2 = 160$ results in a truncation error of less than $-40\,\mathrm{dB}$, which is quite sufficient for practical considerations. Hence, the amount of data in azimuth and elevation is reducible by more than half.

Furthermore, the reconstruction error for varying compression sizes in frequency and joint azimuth-elevation is pictured in Figure 7. A compression size of approx. $N_3 = 40$ and $N_1 = N_2 = 160$ is sufficient for an error less than $-40\,\mathrm{dB}$, why the amount of data in frequency is reducible by approx. 20 times.

Utilising the proposed model order estimation scheme and assuming a significance level $\alpha = 0.01$, the compression sizes are estimated as $N_1 = 164$, $N_2 = 180$ and $N_3 = 72$.

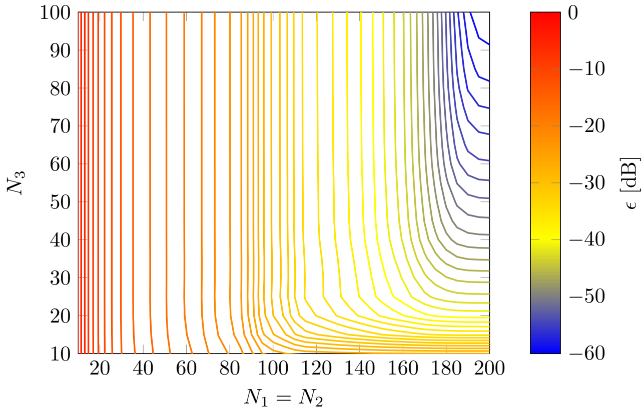


Figure 7. Reconstruction error $\epsilon$ for different compression sizes in joint azimuth-elevation ($N_1 = N_2$) and frequency ($N_3$)

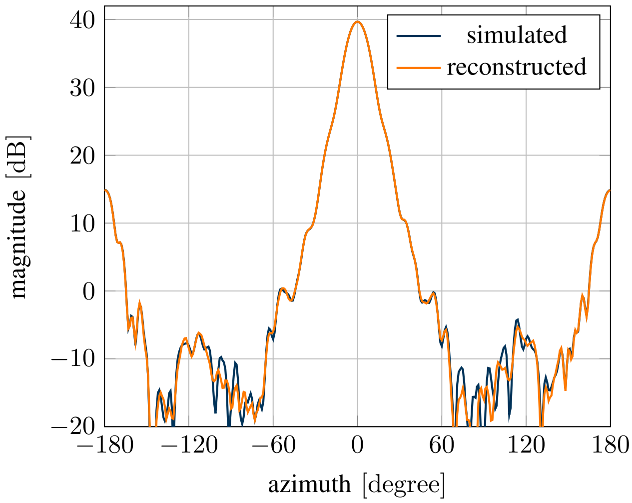


Figure 8. Simulated and reconstructed antenna azimuth cut at elevation 0° and frequency 75 GHz

Taking the aforementioned compression values $N_1 = 160$, $N_2 = 160$ and $N_3 = 40$, we compare simulated and reconstructed antenna pattern cuts. Antenna pattern cuts in azimuth, elevation and frequency are depicted in Figure 8, Figure 9 and Figure 10, respectively. A quite good agreement between simulated and reconstructed antenna pattern is obvious.

## VII. Conclusion

A novel algebraic antenna model ETADF for full 3D interpolation of antenna pattern was presented. Basically, the ETADF extends the known EADF approach to the frequency domain, why the ETADF is a multi-dimensional Fourier transform in azimuth, elevation and frequency. Analytical comparison to other algebraic antenna models was presented. It turned out, that the ETADF requires more coefficients to properly represent the antenna pattern. Nevertheless, this approach is computationally less cumbersome for interpolation purposes. Also, a method to estimate an appropriate model order to sufficiently represent the antenna pattern was presented.

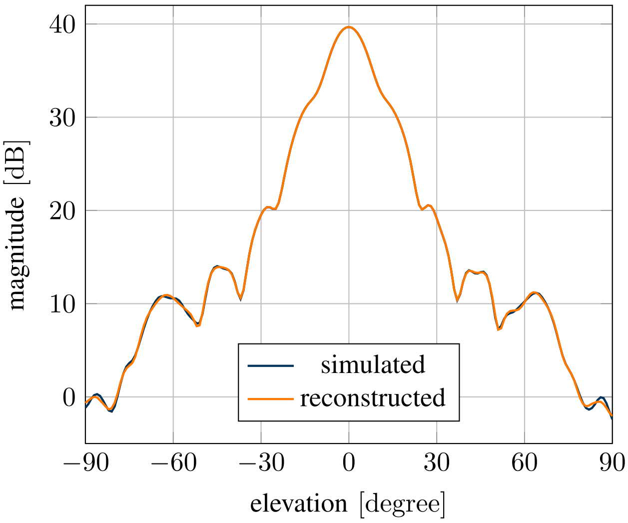


Figure 9. Simulated and reconstructed antenna azimuth cut at azimuth 0° and frequency 75 GHz

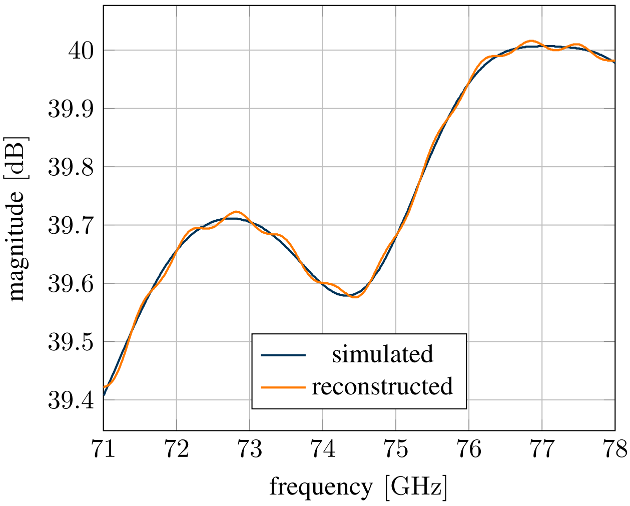


Figure 10. Simulated and reconstructed antenna frequency response at azimuth 0° and elevation 0°

Furthermore, numerically efficient interpolation was derived, which reduces the number of real-valued multiplications approx. by factor 8.

Based on simulation data of a conical horn antenna, the ETADF was verified. The number of Fourier coefficients to sufficiently describe the antenna pattern was reduced by more than half in azimuth and elevation, and 20 times in frequency. Hence, the amount of data to store is significantly reduced and interpolation becomes computationally efficient.

## Acknowledgment


The authors like to thank Dipl.–Ing. Gerd Sommerkorn and Dipl.–Ing. Martin Käske for the fruitful discussions and hints during the preparation of the manuscript.


## References


[1] M. Landmann, M. Kaske, and R. Thoma, "Impact of incomplete and inaccurate data models on high resolution parameter estimation in multidimensional channel sounding," *Antennas and Propagation, IEEE Transactions on*, vol. 60, no. 2, pp. 557–573, Feb 2012.

[2] S. Haefner, M. Kaeske, R. S. Thomae, U. Trautwein, and A. P. Garcia Ariza, "Selection of Antenna Array Configuration for Polarimetric Direction Finding in Correlated Signal Environments," in *WSA 2015; 19th International ITG Workshop on Smart Antennas; Proceedings of*, March 2015, pp. 1–8.

[3] M. Doron and E. Doron, "Wavefield modeling and array processing, part i-spatial sampling," *Signal Processing, IEEE Transactions on*, vol. 42, no. 10, pp. 2549–2580, Oct 1994.

[4] M. Landmann and G. Del Galdo, "Efficient antenna description for mimo channel modelling and estimation," in *Wireless Technology, 2004. 7th European Conference on*, Oct 2004, pp. 217–220.

[5] G. Del Galdo, J. Lotze, M. Landmann, and M. Haardt, "Modelling and manipulation of polarimetric antenna beam patterns via spherical harmonics," in *Signal Processing Conference, 2006 14th European*, Sept 2006, pp. 1–5.

[6] A. Schmitz, T. Karolski, and L. Kobbelt, "Using spherical harmonics for modeling antenna patterns," in *Radio and Wireless Symposium (RWS), 2012 IEEE*, Jan 2012, pp. 155–158.

[7] P. Koivisto, "Reduction of errors in antenna radiation patterns using optimally truncated spherical wave expansion," *Progress In Electromagnetics Research*, vol. 48, pp. 313–333, 2004.

[8] R. Allard and D. Werner, "The model-based parameter estimation of antenna radiation patterns using windowed interpolation and spherical harmonics," *Antennas and Propagation, IEEE Transactions on*, vol. 51, no. 8, pp. 1891–1906, Mar 2003.

[9] W. Dullaert and H. Rogier, "Novel compact model for the radiation pattern of uwb antennas using vector spherical and slepian decomposition," *Antennas and Propagation, IEEE Transactions on*, vol. 58, no. 2, pp. 287–299, Feb 2010.

[10] C. Roblin, "Ultra compressed parametric modelling of uwb antenna measurements," in *Antennas and Propagation, 2006. EuCAP 2006. First European Conference on*, Nov 2006, pp. 1–8.

[11] L. D. Lathauwer, B. D. Moor, and J. Vandewalle, "A multilinear singular value decomposition," *SIAM J. Matrix Anal. Appl*, vol. 21, pp. 1253–1278, 2000.

[12] W. Wiesbeck, G. Adamiuk, and C. Sturm, "Basic properties and design principles of uwb antennas," *Proceedings of the IEEE*, vol. 97, no. 2, pp. 372–385, Feb 2009.

[13] M. Costa, A. Richter, and V. Koivunen, "Unified array manifold decomposition based on spherical harmonics and 2-d fourier basis," *Signal Processing, IEEE Transactions on*, vol. 58, no. 9, pp. 4634–4645, Sep 2010.

[14] J. P. Snyder and U. G. Survey, *Map projections–a working manual*. U.S. G.P.O. : For sale by the Supt. of Docs Washington, 1987.

[15] D. M. Goldberg and J. R. G. III, "Flexion and skewness in map projections of the earth." *Cartographica*, vol. 42, no. 4, pp. 297–318, 2007.

[16] M. Landmann, "Limitations of Experimental Channel Characterisation," Ph.D. dissertation, TU-Ilmenau, Ilmenau, Germany, March 2007.

[17] S. Haykin, Ed., *Adaptive Radar Signal Processing*. New York: Wiley-Interscience, 2007.

[18] B. W. Bader, T. G. Kolda *et al.*, "Matlab tensor toolbox version 2.6," Available online, February 2015. [Online]. Available: http://www.sandia.gov/ tgkolda/TensorToolbox/